Elongated quantum dot as a distributed charge sensor

S. M. Patomäki[1,2,*] J. Williams[1,2] F. Berritta[3] C. Lainé[1,2] M. A. Fogarty[1] R. C. C. Leon[1]
J. Jussot[4] S. Kubicek[4] A. Chatterjee[3] B. Govoreanu[4] F. Kuemmeth[3] J. J. L. Morton[1,2,†] and
M. F. Gonzalez-Zalba[1,‡]

[1]*Quantum Motion, 9 Sterling Way, London N7 9HJ, United Kingdom*

[2]*London Centre for Nanotechnology, University College London, London WC1H 0AH, United Kingdom*

[3]*Center for Quantum Devices, Niels Bohr Institute, University of Copenhagen, Copenhagen, Denmark*

[4]*imec, Kapeldreef 75, Leuven B-3001, Belgium*

Increasing the separation between semiconductor quantum dots offers scaling advantages by facilitating gate routing and the integration of sensors and charge reservoirs. Elongated quantum dots have been utilized for this purpose in GaAs heterostructures to extend the range of spin-spin interactions. Here, we study a MOS device where two quantum dot arrays are separated by an elongated quantum dot (340 nm long, 50 nm wide). We monitor charge transitions of the elongated quantum dot by measuring radiofrequency single-electron currents to a reservoir to which we connect a lumped-element resonator. We operate the dot as a single-electron box to achieve charge sensing of remote quantum dots in each array, separated by an edge-to-edge distance of 480 nm. Charge detection on both ends of the elongated dot at a coinciding setpoint demonstrates that the charge states are well distributed across its nominal length, supported by the simulated quantum mechanical electron density. Likewise, we show elongated-peripheral quantum dot tunnel couplings can exceed 20 GHz, above the electron temperature, fulfilling the requirement for mediated exchange. Our results illustrate how single-electron boxes can be realized with versatile footprints that may enable compact quantum processor layouts, offering distributed charge sensing in addition to the possibility of mediated coupling.

I. INTRODUCTION

In recent years, silicon spin qubits hosted in gate-defined quantum dots (QDs) have achieved major milestones making this platform a compelling option for large-scale quantum computing [1]. These include the demonstration of high-fidelity one- and two-qubit gates on the same device [2–4], high-fidelity readout using rf single-electron transistors (SETs) [5], the demonstration of simple instances of quantum error correction [6] and the scale up to six-qubit devices in a linear arrangement [7]. In addition, chips combining quantum and classical electronics have been

shown to operate at deep cryogenic temperatures, demonstrating a potential route for integrated addressing, control and measurement of qubits [8,9].

Silicon spin qubits typically rely on nearest-neighbor exchange to implement two-qubit interactions [10–12]. Such a short-range qubit coupling applied across the qubit processor leads to high gate densities that hinder integration with local control electronics and gate fan out [13,14], and introduce nonlinear responses due to crosstalk [15]. Furthermore, introducing readout sensors within the qubit plane impacts the level of connectivity that can be achieved. To scale up beyond one-dimensional qubit arrays and integrate cryogenic electronics requires structures with enhanced functionality, which can increase the separation between qubits, or between qubits and sensors. One approach to scaling is to use dispersive charge sensors, such as the rf single-electron box (SEB) [16–19]. The SEB offers similar levels of sensitivity to conventional charge sensors [20,21] but requires only one charge reservoir, as opposed to two for the SET, facilitating the design of qubit arrays with higher connectivity. Another approach is to space out qubits by using elongated quantum dots (EQDs) to mediate exchange interactions between

———————
*Corresponding author: patomaki@mit.edu, sofia@quantummotion.tech

†Corresponding author: john@quantummotion.tech

‡Corresponding author: fernando@quantummotion.tech

them [22–24]. Such an approach, requiring tunnel coupling between each of the remote QDs and the EQD, has been demonstrated in GaAs heterostructures to mediate fast, coherent exchange interaction between single spins separated by half a micron [25]. A further advantage of the EQD is that it could itself act as a local charge reservoir to facilitate initialization [26].

In this paper, we combine aspects of these two concepts to demonstrate an SEB with an elongated charge island that enables charge sensing of multiple remote QDs, which, due to the increased separation, show minimal crosstalk. The structure is fabricated using a three-layer n^+-doped polycrystalline silicon gate MOS process that enables the formation of the elongated SEB as well as few-electron QDs. The extended distribution and quantization of the charge within the EQD, consistent with semiclassical modeling, allows it to sense the charge on QDs separated by over 0.5 μm. Finally, we show tunnel coupling between the remote QDs and the EQD, which fulfills one of the requirements for coherent mediated exchange.

II. EXPERIMENTAL METHODS

Our device consists of two double quantum dots (DQDs) separated by an EQD, nominally 340 nm long and 50 nm wide. The measured device is fabricated with three 30-nm-thick *in situ* n^+ phosphorus-doped polycrystalline silicon gate layers formed with a wafer-level electron-beam patterning process. A high-resistivity (>3 kΩ/cm) p-type Si wafer is used, on which a 8-nm-thick, high-quality SiO_2 layer is grown thermally to minimize the density of defects in the oxide and at the interface. Gate layers are electrically isolated from one another with a 5-nm-thick blocking high-temperature deposited SiO_2 [27]. A schematic of the measured device is shown in Fig. 1(a). We employ one layer of gates (closest to the silicon substrate) to provide confinement for the three possible current paths connecting Ohmic contacts, around the active region of the device. A second layer of gates is used to form barriers between the EQD, the QDs, and the reservoirs. As seen in other MOS QD arrays [28], QDs can also be formed under these "barrier" gates in the second layer, depending on applied gate voltages. A third gate layer is used as plungers to control the occupation of the EQD, the QDs, and the extension of two-dimensional electron gases (2DEG) from under accumulation gates, denoted as reservoir (R), source (S), and drain (D), overlapping with corresponding Ohmics, towards the active region of the device.

The device is cooled down in an Oxford Instruments Triton dilution refrigerator equipped with QDevil DACs, thermalizing filters and high-bandwidth sample holders [29]. At base temperature (25 mK), we confirm the functionality of the device with gate-electrode leakage tests, followed by pinch off and saturation voltage measurements
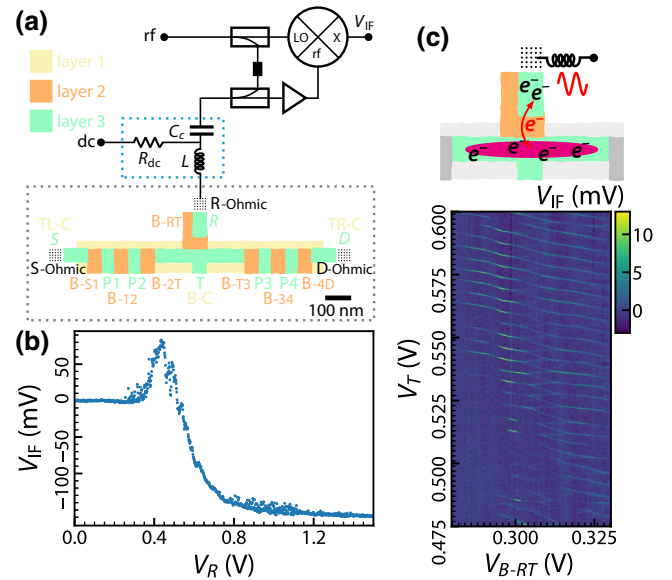

FIG. 1. Formation of an elongated single-electron box. (a) Device schematic (gray dotted rectangle) with simplified rf circuit diagram (signal filtering omitted). A lumped-element resonator (blue dotted rectangle) is galvanically attached to the Ohmic contact below the accumulation gate R and monitored via changes in the demodulated baseband-frequency reflectometry signal, V_{IF}. (b) Changes in V_{IF} reflect the accumulation of a 2DEG with increasing reservoir gate voltage V_R. All other gates are held at zero bias. (c) The EQD is operated as a single-electron box. Here, gates at zero bias are drawn in grayscale, while biased gates are drawn in color. Magenta blobs are sketches indicating locations of QDs of interest. An elongated, multielectron quantum dot forms under gate T and is tunnel coupled to a charge reservoir accumulated under gate R. Driving the resonator at its natural frequency drives cyclic electron tunneling between the reservoir R, and the elongated quantum dot under gate T. The (T, B-RT) stability diagram obtained at $V_R = 1.5$ V shows dot-to-reservoir transitions that become increasingly regular with increasing V_T. The signal strength depends on $V_{B\text{-}RT}$, since the barrier voltage modulates the EQD-reservoir tunnel rate.

(see Appendix A for the preliminary device characterization protocol).

We detect charge transitions between the EQD and the reservoir using rf reflectometry [30], via a lumped-element resonator attached to the Ohmic contact of the accumulation gate R, as illustrated in the inset of Fig. 1(c). Further details of the rf reflectometry setup and data acquisition are presented in Appendix B. The rf voltage V_{rf} drives single-electron ac tunneling currents between the reservoir and the EQD when not in Coulomb blockade. Cyclic tunneling manifests as changes in the complex impedance of the device, modifying the resonant frequency and matching impedance of the lumped-element resonator [31]. We apply a signal with frequency close to that of the resonator and the reflected signal, which carries information of the complex impedance of the SEB, is amplified and mixed
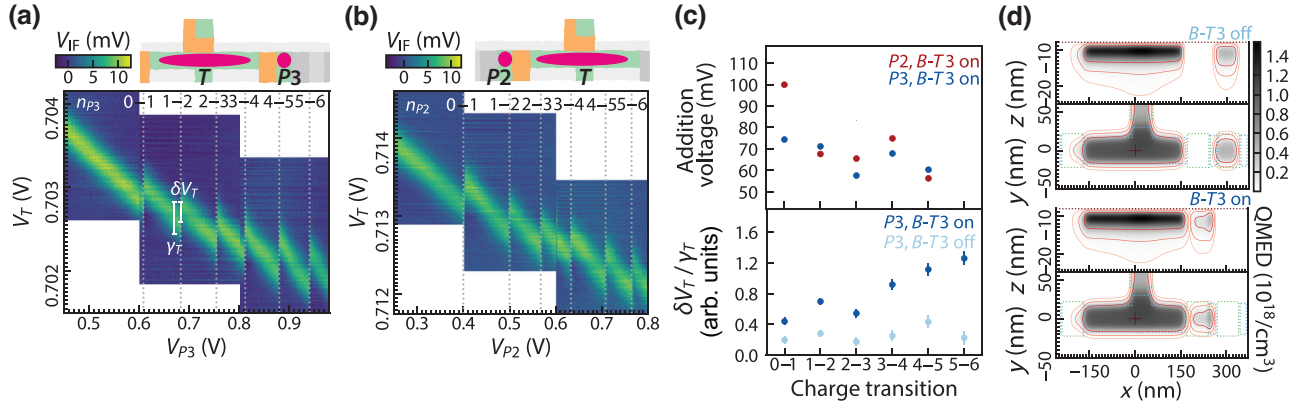
FIG. 2. Charge sensing of QDs under $P2$ and $P3$. Operating point (top schematic) and discontinuities in the SEB peak locations (bottom dataset) reveal electron loading voltages for (a) $P2$ and (b) $P3$ (white numbers). (c) Upper panel shows the addition voltages extracted from (a) and (b). Error bars, obtained from V_{P2} and V_{P3} resolution, are smaller than marker size. (c) Lower panel shows the sensor peak shift, δV_T, with respect to peak linewidth, γ_T, at $P3$ QD charging events with B-$T3$ on [isolated from drain, as in (b)] and B-$T3$ off (connected to the reservoir formed with gate D). (d) Simulated QMEDs along constant y and z of the T-$P3$ DQD with B-$T3$ at zero bias (top panel); and biased with a positive voltage (bottom panel) are shown as grayscale colormaps overlayed with layer 2 (green) and 3 (blue) gate locations (dotted rectangles). Red contours correspond to $t(1 - m\sigma)\rho_{\max}$ for $m = 1, 2, 3$. Gate side view (top) highlights the locations of gates T and B-$T3$.

III. RESULTS

A. Single-electron box tune up

In order to operate the EQD as an SEB, we extend a 2DEG close to the active region of the device from a nearby Ohmic contact by applying a positive voltage to gate R. We bias the EQD plunger gate, T, above the pinch-off voltage and tune the tunnel rate between the reservoir and the EQD by adjusting the voltage on the barrier gate B-RT. To tune the SEB, we first record V_{IF} as a function of V_R [see Fig. 1(b)]. As V_R is increased, V_{IF} changes as the 2DEG is formed, modifying the circuit impedance. For $V_R \gtrsim 1$ V, V_{IF} is nearly constant, indicating that the 2DEG is fully accumulated. In this region, changes in the resonator response due to voltage sweeps on the other gates can be ascribed to ac charge transport between the QDs and the 2DEG in the reservoir.

Having fixed $V_R = 1.5$ V, we then map out the charge-stability diagram between gates T and B-RT [Fig. 1(c)], which shows dot-to-reservoir transitions (DRTs) indicating the presence of discretized charge states. For $V_T \lesssim 0.55$ V, the data suggest a complex system comprising at least two coupled QDs, while for $V_T \gtrsim 0.55$ V, the stability diagram increasingly resembles that of a single QD. Selecting $V_{B\text{-}RT} = 0.29\dots0.31$ V maximizes the signal V_{IF}

due to optimal tunnel rates between the reservoir and EQD. In the following, we use $V_T = 0.69\dots0.72$ V, which we show to be sufficient for the EQD to extend over the length of the gate T.

B. Charge sensing of quantum dots

We next use the EQD as an SEB to individually sense electrons in QDs under $P2$ and $P3$, and also as a local electron reservoir for these dots [see Figs. 2(a) and 2(b)], by biasing the device at operating points **O1** and **O2** (see Appendix C, Table I), as illustrated in Figs. 2(a) and 2(b).

Barrier gate voltages are chosen to reside below their observed first electron loading voltages, based on (B-$2T$, T) and (T, B-$T3$) stability diagrams (data not shown). We detect the loading of an electron to either $P2$ or $P3$ QDs as a discontinuity in the SEB DRT, caused by the mutual capacitance between the EQD and the QDs. We mark the $0 \rightarrow 1$ charge transitions as the first detected discontinuity. We find the first electrons to load at $V_{P2}(0 \rightarrow 1) = 0.400$ V, and $V_{P3}(0 \rightarrow 1) = 0.609$ V, respectively, a difference of 0.21 V. Subsequent electrons load in steps of tens of millivolts. At occupancy of one electron, we find typical sensor peak voltage SNRs of $\text{SNR}_{P2} = 10.7$ and $\text{SNR}_{P3} = 14.6$, using an integration time of 1 ms (see Appendix B for details).

In order to understand whether the sensed QDs $P2$ and $P3$ are in the few-electron regime [32], we plot the extracted addition voltages in Fig. 2(c). These addition voltages carry information of the electron-number-dependent confinement energies, as $V_g(n_d \rightarrow n_d + 1) - V_g(n_d - 1 \rightarrow n_d) = \alpha_{dg}^{-1}[E_{Cd}(n_d) + \Delta(n_d)]$, where n_d is the electron number at the QD d; α_{dg} is the lever arm from
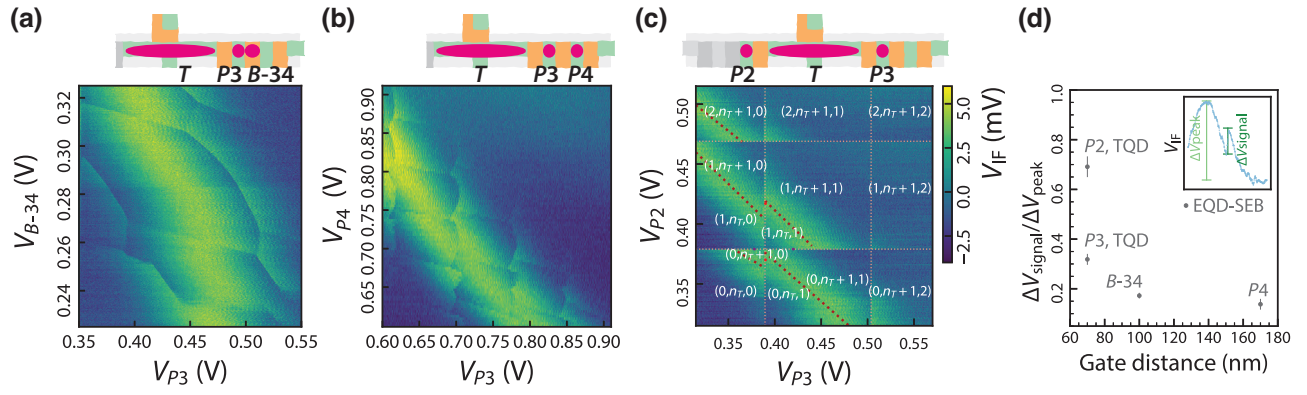
FIG. 3. Elongated single-electron box as a distributed sensor. (a)–(c) SEB charge-sensed stability diagrams of DQDs controlled with gates (a) $P3$ and B-34, (b) $P3$ and $P4$, and (c) TQD controlled with gates $P2$, T, and $P3$. Gate biasing and QDs are sketched with device schematics above the color maps. (a) To define a DQD under $P3$ and B-34, we extend a 2DEG from the reservoir formed under gate D. We bias B-4D in saturation, and $P4$ near its pinch off. (b) To define a DQD under $P3$ and $P4$, we instead bias B-34 and B-4D as barriers. (c) To define a TQD between $P2$, T, and $P3$, we bias B-2T, B-$T3$, and B-34 as barriers. We bias $V_T = 0.7093$ V to obtain a signal near the first $P2$ and $P3$ QD electrons. The estimated $P2$, T, and $P3$ QD charge occupations are indicated as (n_{P2}, n_T, n_{P3}). (d) Sensitivity as a function of sensor-QD gate distance, with data extracted from panels (a)–(c).

QD d to gate g; and $E_{Cd}(n_d) + \Delta(n_d)$ is the sum of the corresponding on-site charging energy and the confinement energy. The addition voltages are irregular in general and, in particular, we observe an increase in the addition voltage both for $P2$ and $P3$ when loading from the presumed $4 \to 5$ electron state. This is consistent with filling the lowest two $\pm z$ valley-orbit states, such that the next electron occupies a higher-energy orbital state.

In Fig. 2(c), we show the shifts in V_T induced by $P3$ electron loading, δV_T, relative to the fitted linewidth of the SEB DRT, γ_T. This ratio $\delta V_T/\gamma_T$ is a proxy for charge sensitivity, and indicates whether the sensor is in the small or large signal regime [33]. When loading from the EQD, with $V_{B\text{-}T3} = 0.225$ V, the shifts become larger than the linewidth of the sensor peak, i.e., $\delta V_T \geq \gamma_T$, by the fifth electron. We retain some sensitivity to the QDs even when the barrier gates to the EQD are off at zero bias. In this case, we resort to loading electrons under $P3$ from a reservoir formed via D (see **O3** from Table I).

The first $P3$ electron shifts the sensor by approximately 0.4 linewidths, which corresponds to a drop in signal such, that $\Delta V_{\text{signal}}/\Delta V_{\text{peak}} = 0.32$, and SNR = 2.9. As we have

$t_{\text{int}} = 1$ ms, we have a minimum integration time $t_{\text{min}} = 0.12$ ms for single-shot readout. For a full peak shift, we expect $t_{\text{min}} = 4.7$ μs, which could be improved further by using low-loss microwave frequency resonators [34] and Josephson parametric amplifiers [35]. We note that the first electron under $P3$ at this operating point is found at $V_{P3} = 0.387$ V. We find that in this operating point, the sensitivity is lower and increases more slowly.

To qualitatively illustrate the effect of the barrier gates, we employ a self-consistent Schrödinger-Poisson solver (SPS) from a three-dimensional nanostructure simulation software [36,37] to evaluate so-called quantum mechanical electron densities (QMEDs), denoted with $\rho(\mathbf{r})$. We assimilate the QMEDs to probability densities under QDs to estimate shapes of many-electron charge states (see Appendix E for details of the simulation methods). Figures 4(e) and 4(f) show the (x, z) (top), and (x, y) (bottom) plane views of the simulated QMEDs of the T-$P3$ system studied in Figs. 2(b)–2(d). The two QMEDs are simulated by biasing the QD plunger gates (T or $P3$), and nearest-neighbor barrier voltages at the nonzero biases where experimental data was taken. In the simulations, the barriers modify the

TABLE I. Operating points. **O1**–**O3** correspond to the setpoints of the data in Figs. 2(a)–2(c). **O4**–**O6** correspond to the setpoints of the data in Figs. 3(a)–3(c). Numbers in parentheses refer to the voltages used in a simulation.

| Operating point	V_R	$V_{B\text{-}RT}$	$V_{B\text{-}12}$	V_{P2}	$V_{B\text{-}2T}$	V_T	$V_{B\text{-}T3}$	V_{P3}	$V_{B\text{-}34}$	V_{P4}	$V_{B\text{-}4D}$	V_D
O1	1.5	0.29	0.0	varies (0.4)	0.25	varies (0.712)	0.225	0.0	0.0	0.0	0.0	0.0
O2	1.5	0.29	0.0	0.0	0.25	varies (0.703)	0.225	varies (0.609)	0.0	0.0	0.0	0.0
O3	1.5	0.295	0.0	0.0	0.25	varies (0.709)	0.0	varies (0.388)	0.275	0.9	0.9	1.5
O4	1.5	0.295	0.0	0.7	0.25	0.7084	0.0	varies	varies	0.9	0.9	1.5
O5	1.5	0.295	0.0	0.0	0.0	0.7068	0.0	varies	0.275	varies	0.275	1.5
O6	1.5	0.295	0.0	varies (0.45)	0.25	0.7093	0.0	varies (0.45)	0.275	0.9	0.9	1.5
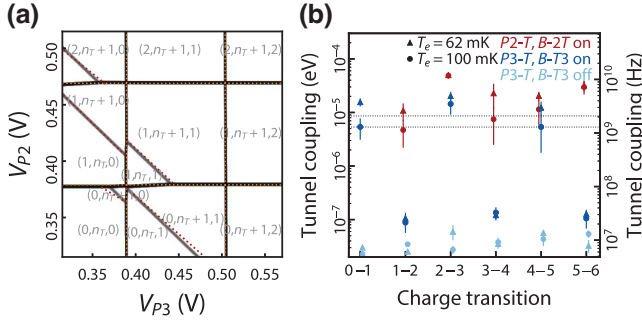
FIG. 4. Triple quantum dot parameters. (a) Grayscale colormap shows the sum of voltage curvatures of the ground state of an electrostatic Hamiltonian, obtained using the experimentally estimated lever arms and charging energies. Orange and red dotted lines correspond to the fitted lines from Fig. 3(c). (b) Estimates for the T-$P3$ and T-$P2$ tunnel couplings are shown as triangles for fixed $T_e = T_e^{\text{best}} = 62$ mK, and $T_e = T_e^{\text{upper}} = 100$ mK with triangle and round markers, respectively. The datasets are offset from one another by ± 0.05 on the x axis for clarity.

shapes of the QDs, pulling QDs controlled with plunger gates towards the biased barriers, and extending the shape of the EQD. As we discuss below, the QD shape and location also impacts, e.g., lever arms.

C. Charge-sensing coupled quantum dots

Having established the basic operation of the EQD as an SEB charge sensor for nearby QDs, we next demonstrate its ability to sense different configurations of nearby coupled QDs. We then go on to assess the sensitivity of this distributed charge sensor with increasing distance. First, we form a DQD under $P3$ and B-34 by biasing at **O4** from Table I, and retune the sensor at the center of V_{P3} and $V_{B\text{-}34}$ voltage ranges. The resulting SEB-sensed ($P3$,B-34) stability diagram is shown in Fig. 3(a). We observe a honeycomb pattern typical for a tunnel-coupled DQD, retaining sensitivity to charge transitions of both QDs, at an edge-to-edge distance B-34 to the EQD of 100 nm. We measure local addition voltages of approximately 114 ± 1 mV and 43 ± 1 mV for $P3$ and B-34, respectively.

Second, we form a DQD under $P3$ and $P4$ [see Fig. 3(b), and **O5** from Table I]. Here, the DQD honeycomb pattern has average addition voltages of approximately 77 ± 5 and 63 ± 5 mV for $P3$ and $P4$, respectively. The observation of latching [38], i.e., distortion of $P3$ charge transitions, suggest that $P3$-$P4$ or $P4$-D tunnel rates are of the order of the ramp frequency f_{ramp} (see Appendix B for details on data acquisition). The edge-to-edge distance of $P4$ to the EQD is nominally 170 nm.

Finally, we form a triple quantum dot between $P2$, T, and $P3$, by biasing at **O6** from Table I. Figure 3(c) shows the resulting ($P2$,$P3$) charge-stability diagram of the triple QD. We label the estimated charge configuration for the $P2$, T, and $P3$ system as (n_{P2}, n_T, n_{P3}). The operating point

is close to a so-called hextuple point, characterized by the hourglass shape, formed between $(0, n_T + 1, 0)$ and $(1, n_T, 1)$ charge states [39]. This demonstrates sensitivity over an edge-to-edge distance of 480 nm, going beyond the range of sensitivity of conventional SEBs or SETs [7].

We plot an estimated sensitivity as a function of sensor-QD distance in Fig. 3(d). Here, sensor-QD distance refers to the shortest edge-to-edge gate-gate distance, between the gates used to control the sensor and the QD. In order to benchmark a measurement setup independent sensitivity, which depends only on the sensor device, the sensitivity is extracted as $\Delta V_{\text{signal}} / \Delta V_{\text{peak}}$ from data in Figs. 3(a)–3(c), for each of the sensed QD. Hence, no simulations to estimate the QD location were used. As can be observed from the difference between sensitivities to the $P2$ and $P3$ QDs (0.69 and 0.32, respectively), which are nominally at the same distance from the sensor, the barrier voltage affects the effective distance. We find that the sensitivity falls off to approximately $\Delta V_{\text{signal}} / \Delta V_{\text{peak}} = 0.1 \ldots 0.2$ as the gate distance is increased to approximately above 100 nm, and that we retain sensitivity up to (nominal) distances of 170 nm.

To confirm our understanding of the locations of the QDs in the triple QD configuration above, we extract the various lever arm ratios from the slope of the SEB peak and the quasivertical and horizontal charge-sensing shifts, obtained by line fits to the SEB peak positions (see Appendix F). We observe close to zero $P2$-$P3$ crosstalk, as expected for remote QDs, with the estimate $\alpha_{P3,P2}/\alpha_{P3,P3} = (8 \pm 6) \times 10^{-3}$, obtained from the $P3$ charge transitions as a function of V_{P3}. We get $\alpha_{P2,P3}/\alpha_{P2,P2} = 0 \pm [0, 3.33 \times 10^{-3}]$, limited by the lower data resolution along the V_{P2} axis. The average of the fitted EQD DRT slopes, marked with dashed dark red lines, is $\alpha_{T,P3}/\alpha_{T,P2} = 0.65 \pm 0.11$. A ratio equal to 1 would indicate an EQD wave function, which is symmetric with respect to locations of gates $P2$ and $P3$. Intuitively, the positively biased barrier B-$2T$ ($V_{B\text{-}T3} = 0$ V) pulls the EQD electron wave function towards $P2$, which could explain the lever arm asymmetry.

Overall, the data from Fig. 3(c) demonstrates the readout of QDs that are separated by approximately 510 nm center-to-center, using the elongated SEB as a distributed charge sensor. The fact that a single EQD charge transition is capacitively shifted by the addition of charges to either $P2$ or $P3$ at the same EQD bias conditions demonstrates that the EQD extends approximately over the length of gate T.

D. Towards mediated exchange

We have demonstrated utilizing the EQD as a a charge sensor, an electron reservoir, and a spacer that reduces crosstalk between qubits. One of the main expected uses of EQDs are as coherent qubit couplers. Requirements for

mediated exchange include level spacings above thermal energy, and strong EQD-QD tunnel coupling [23]. In addition, the level spacings and tunnel couplings determine the strengths of state leakage and seepage processes [40], which limit the fidelity of the resulting mediated exchange operation. At $T_e = 100$ mK, assuming $m^* = 0.2m_e$ [41], level spacings for a particle in a box predict an upper EQD length limit of $\ell = 660$ nm. We may experimentally estimate the attainable mediated exchange strength in our devices by quantifying the lever arms, capacitances, and tunnel couplings of the ($P2$,T,$P3$) triple quantum dot (TQD).

We estimate the lever arm components of the ($P2$,T,$P3$) system from the lever arm ratios from four datasets (see Figs. 2–3). These are converted to lever arms using an $\alpha_{T,T}$ estimated from another device by measuring the T addition voltage of $|e|^{-1}\alpha_{TT}^{-1}E_{CT} = 4.4 \pm 0.2$ mV (see Appendix D). In addition, we simulate the lever arms in the experimental operating points to benchmark our quantitative understanding. The measured and simulated parameters are valid locally in voltage space. They depend on the operating point (see Table I) due to operation of $P2$ and $P3$ in the few-electron regime, and due to the barrier-gate tuneability discussed in Sec. III B. This procedure (see Appendices F and G) yields the experimental lever arm matrix, the relative experiment-simulation error matrix, and the inverse capacitance matrix of

$$\boldsymbol{\alpha} = \begin{pmatrix} 12.20 & 4.99 & 0.01 \\ 0.66 & 92.60 & 0.49 \\ 0.07 & 4.99 & 9.01 \end{pmatrix} \times 10^{-3}, \qquad (1)$$

$$\boldsymbol{\delta\alpha} = \begin{pmatrix} 1.43 & 5.29 & 14.2 \\ 0.674 & 1.99 & 0.327 \\ 0.593 & 0.074 & 2.12 \end{pmatrix}, \qquad (2)$$

$$|e|\,(\mathbf{C}_{dd})^{-1} = \begin{pmatrix} 0.463 & 0.014 & 10^{-5} \\ 0.014, & 0.407 & 0.004 \\ 10^{-5} & 0.004 & 0.697 \end{pmatrix} \times 10^{-3}. \quad (3)$$

Simulated lever arms are systematically larger compared to experimentally extracted values, albeit typically agreeing within an order of magnitude, and correctly describing trends associated with, e.g., barrier gate voltages [see Fig. 8(f) for illustration]. We find the largest errors for $\alpha_{P2,P3}$ and $\alpha_{P2,T}$ (14.2 and 5.3, respectively), while the remaining off-diagonal lever arms have the smallest errors, from 0.074 to 0.67. The reason for systematically larger simulated lever arms has not been confirmed, but we suspect that the absence of the electron reservoirs in the simulation may play a role (see Appendix E for discussion).

The lever-arm matrix confirms charge configurations for the data from Fig. 3(c) via a stability diagram simulation. The resulting sum of ground-state energy curvatures along gate voltages, $d^2E_g/dV_{P2}^2 + d^2E_g/dV_{P2}^2$, is

shown in Fig. 4(a). The simulation displays qualitative agreement with data, and confirms the charge configurations (n_{P2}, n_T, n_{P3}). The measured sensor slope in the (n_{P3}, n_{P2}) = (1, 1) is $a_T = -0.703 \pm 0.008$, while the choice of lever arm matrix in the simulation leads to $a_T = -0.739$. The experimental and simulated ($P2$,T) charge-induced voltage shifts along V_{P2} agree within experimental resolution of ± 1 mV, $\Delta V_{P2} = 13 \pm 1$ mV.

We estimate the EQD-$P2$ and EQD-$P3$ tunnel couplings at operating points **O1** and **O2** from data shown in Figs. 2(a)–2(c) by fitting the thermal equilibrium charge expectation value across each ICT [42]. See Appendix I for the methods. The resulting measured tunnel couplings for each of the three datasets are gathered in Fig. 4(b), evaluated at fixed temperatures of $T_e = 62(100)$ mK. Here, 62 mK is the best estimate, and 100 mK is an upper bound. The tunnel coupling estimates generally decrease with increased temperature, but the average difference between the temperatures is below 6.6 μeV, 3.2 neV, and 3.8 μeV, respectively, for the T-$P2$, T-$P3$ (B-$T3$ off), and T-$P3$ (B-$T3$ on) datasets.

We observe that B-$T3$ modulates the T-$P3$ tunnel coupling. When B-$T3$ is off, we measure $t_{T,P3} = 40$ (37) neV averaged over the charge transitions, which we expect to be limited in precision by the SNR. We indicate the average at $T_e = 62$ mK first, and at $T_e = 100$ mK in parentheses. At $V_{B\text{-}T3} = 0.225$ V, the estimated tunnel couplings are orders of magnitude higher, although the change is charge transition dependent. For even-to-odd charge transitions, $t_{T,P3} = 16$ μeV (8.4 μeV), while for odd-to-even, $t_{T,P3} = 0.12$ μeV (0.11 μeV). Since the trend follows the charge-transition parity, it could be explained by electron orbitals. An equally clear effect is not visible for the T-$P2$ tunnel couplings, for which we have $t_{T,P2} = 27$ μeV (20 μeV), with a difference between even-to-odd and odd-to-even tunnel couplings of 13 μeV. The parity "rule" breaks for the (5)–(6) charge transition. We suspect that a role is played by how the QDs are shaped by the barrier gate voltages.

Based on these extracted parameters, we numerically estimate the mediated exchange strength and the state and seepage leakage errors, see Appendix J for details of the simulation. We find that the exchange strength is correlated with state leakages, such that faster operation is associated with higher leakages, and hence lower fidelity. For example, we find detunings where the mediated exchange could exceed 1 GHz but the associated leakage rates will be well above fault-tolerant thresholds, indicating that dynamics such as nearest-neighbor tunneling dominates at such operating points. At resonance $\epsilon_T = \epsilon_{P2}, \epsilon_{P3}$, we find $J_{121} = -17$ MHz, with a lower state leakage out and into the computational subspace of 0.03 and 0.01, respectively. Conversely, at $J_{121} = -1$ MHz, we estimate leakage rates out plus in of 0.012, which is closer to the typical surface-code error threshold of 0.01. It may

be possible to engineer the leakage rates with, e.g., the EQD geometry, which affects the charging energies. We note estimated exchange range from one to tens of MHz compares well with state-of-the-art planar SiMOS devices with 1–10 MHz nearest-neighbor exchange [43]. Overall, our measured tunnel couplings and estimated exchange strengths indicate that the mechanism could be useful for two-qubit gates in the SiMOS platform.

IV. OUTLOOK

We have used the EQD as a rf-SEB charge sensor capable of sensing QDs up to 355 nm away from the EQD center, suggesting that the same SEB charge state may be sensitive to charges in QDs separated by over 700 nm. Further, in the case the charge-sensing events producing a sensor peak shift from its maximum to the background noise level, we find a minimum integration time of 5 µs (defined as the integration time to achieve a SNR = 1). We predict that number could be brought down to 200 ns when using a 1 GHz resonator and down to 20 ns when used in conjunction with a Josephson parametric amplifier. Our results are well supported by quantum mechanical electron density simulations. The enhanced functionality provided by the EQD may be expanded in future QD-based architectures to sensors defined with more complex gate shapes, such as a right angle, a cross, or a T shape. Such sensors could allow sensing two, three, and four QDs placed around the periphery, covering unit cells in qubit grids with, e.g., lattice and weave connectivities [20], enabling alternative unit cells requiring fewer individual gate structures for readout. Combined with the demonstration of few-electron QDs, our results show the potential of this multigate polysilicon platform to produce scalable QD unit cells.

Another potential application of this type of elongated QD is as a midrange spin-qubit coupler as previously demonstrated for QDs in GaAs/(Al,Ga)As heterostructures [25]. Here, we have demonstrated two basic requirements towards this application: the quantization of charge in the EQD up to EQD lengths of 1 µm, and barrier gate tuneable tunnel couplings to QDs at the periphery up to several GHz, above the estimated electron temperature. We expect mediated exchange in a device with similar parameters to reach above MHz over a range of detunings. We anticipate state leakage errors of around 3%, which may limit the fidelity of the operation. Other possible uncertainties include the lack of information on the orbital spacing, which needs to exceed the electron temperature. We envision that extended QDs could become a key resource to increase the range of qubit-qubit interaction in silicon, complementing other approaches such as spin shuttling [44–46], capacitive coupling with floating gates [47,48], and microwave photonic links [49,50]. Additionally, we have shown that the EQD can be used as a local electron reservoir, which can be utilized in schemes mitigating charge leakage errors [26]. Many practical qubits in platforms ranging from superconducting to neutral atoms have leakage states [51,52], and control protocols for higher-fidelity operation are an active field of research. Here we highlight the need to establish that discussion in the framework of spin qubits coupled to EQDs.

ACKNOWLEDGMENTS

APPENDIX A: CRYOGENIC DEVICE CHARACTERIZATION

To assess operability of the device measured in the main text, labeled as device **A**, we measure gate leakage conductances, and pinch off and saturation voltages at the base temperature of the cryostat. Gate leakages are measured by applying an increasing voltage to gate g_i while measuring current through all channels, and repeating for all gate electrodes i. Leakage conductance l_{ij} is taken as the average conductance over the voltage range. The resulting leakage matrix is shown in Fig. 5(a). The device under study has leakage currents no larger than ± 1.3 pA/V at cryogenic temperatures.

The first guess for Coulomb blockade operating point is obtained from gate pinch off and saturation voltage measurements, where we operate the device similarly to a circuit of classical MOS field-effect transistors in series. The device has three possible current channels: source-drain, reservoir-source, and drain-reservoir. Pinch-off voltages are measured by applying a $V_{oi-oj} = 1$ mV between Ohmics oi and oj along channel $i - j$, and by biasing all layer 2 and 3 gates along said channel at 2.0 V. The gate voltage of one of those gates is swept from 2.0 V to -0.5 V and back while recording current. Pinch-off and saturation voltages are defined as the voltages where measured current is 5% and 90% of the saturation current, respectively. If saturation is not observed, pinch-off current is defined as 5% of the maximum measured current.

In this device, all three channels are functional. A summary of the results, obtained by biasing the source-drain, source-reservoir, and drain-reservoir channels, are shown in Figs. 5(b) and 5(c). The accumulation gates source (S), reservoir (R), and drain (D) saturate at higher
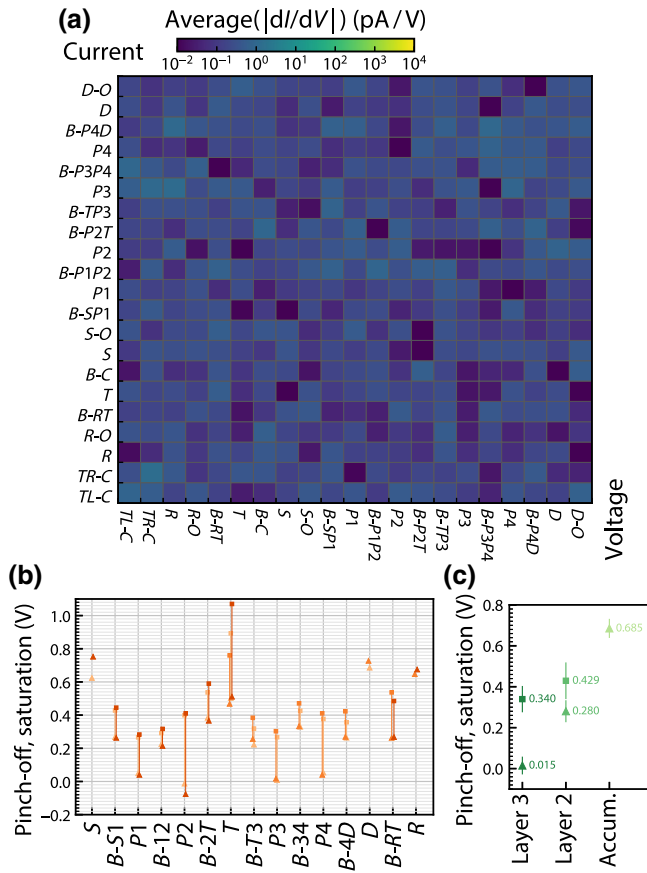
FIG. 5.   Leakage currents, pinch-off, and saturation voltages. (a) Leakage matrix, where the color of a pixel shows the average conductance between gate i (matrix columns), where we apply a voltage, and channel j (matrix rows), where we read out current. Applied voltage ranges from -4.8 to $+4.8$ mV. (b) Summary of pinch-off and saturation voltages for all gates. Colors from dark to light correspond to current measured through the S-D, S-R, and D-R channels, respectively. (d) Gate-type-wise summary of average pinch-off and saturation voltages for data in panel (b), where average values are denoted with the same markers as panels (a)–(c), and error bars denote standard deviations. Layer 3 coincides with plunger gates, where the T-plunger gate has been left out due to significantly different size. Layer 2 coincides with barrier gates. Accumulation gates are also on layer 3.

voltages than other gates. Other layer-3 gates systematically require a larger voltage range between pinch off and saturation than layer-2 gates. This observation is consistent with the increasing total oxide thickness with increasing layer index. Hysteresis was not observed in this device.

APPENDIX B: RADIOFREQUENCY REFLECTOMETRY AND DATA ACQUISITION

Figure 6 shows a schematic of the rf reflectometry setup for biasing the lumped-element resonator attached to the Ohmic of the accumulation gate R, and acquiring the
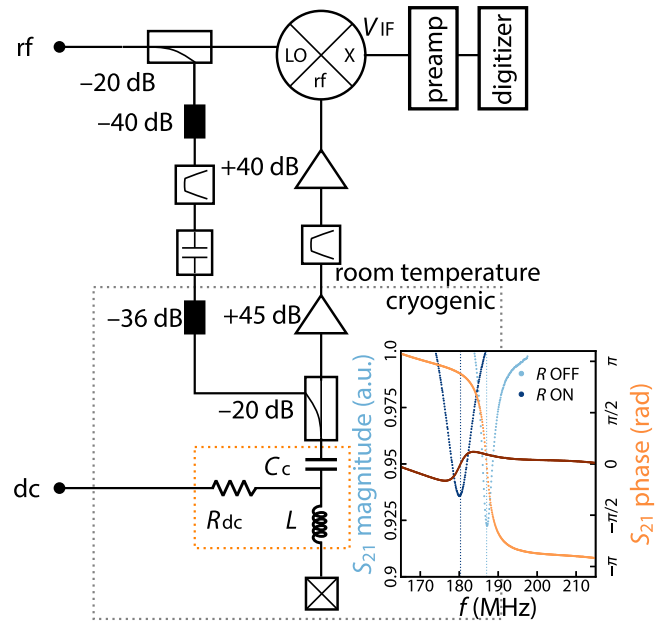

FIG. 6.   Radiofrequency reflectometry. Simplified cryogenic and room-temperature rf setup, with a lumped-element resonator (circuit bordered with orange dotted rectangle) attached to the Ohmic of the accumulation gate R (crossed square). Attenuation is performed in stages inside the cryostat. The total attenuation of -36 dB is shown for simplicity. dc filtering is not shown. Embedded plot shows the resonator response in a vector network analyzer reflection measurement, in which the input and output signal are split for attenuation and cryogenic amplification. Signal magnitude is shown as blue datapoints up to a 6-dB bandwidth. Signal phase is shown as orange datapoints. Datasets with the accumulation gate R off at zero bias are plotted as lighter datasets, and datasets with gate R on at positive bias as darker datasets. Estimated resonance frequencies are denoted with dotted lines.

reflected signal. The diagram includes attenuation, amplification, and the key components. Here, $R_{dc} = 49.99$ kΩ, $L = 820$ nH, and $C_c = 22$ pF. There is also an overall coupling capacitor of 100 pF in series with C_c, omitted for simplicity.

All device gates are connected to dc lines (not shown), which are biased with a voltage digital-to-analogue converter (DAC). To acquire a trace or a stability diagram, the DAC is programmed to send one- or two-dimensional step-discretized voltage ramps, with a step taking $t_{sample} = 10^{-4}$ s corresponding to ramp frequency $f_{ramp} = 10$ kHz. The start of the ramp is synchronized to a trigger sent to the digitizer. We digitize V_{IF} using a sample rate of 1 MS/s, with the voltage preamplifier low-pass cutoff $f_{low\,pass} = 10$ kHz. We boxcar filter the trace with a window size corresponding to t_{sample}, and decimate accordingly to get a t_{sample}-spaced dataset. We average by repeating acquisition $n_{average} = 10$ times. Hence, we estimate the integration time $t_{integrate} = n_{average}/f_{low\,pass} = 1$ ms.

Embedded to Fig. 6 is the vector network analyzer (VNA) response with the gate R (and the entire device) at zero bias (light blue and light orange datasets for magnitude and phase responses), and with the gate R on (dark blue and dark orange datasets, respectively). The resonator responds both by changing its resonance frequency and coupling coefficient—we observe the resonance frequency and the coupling coefficient to decrease, taking the resonator from overcoupled to undercoupled as a 2DEG is accumulated under gate R.

APPENDIX C: OPERATING POINTS

Operating points used with the data presented in the main text are summarized in Table I.

APPENDIX D: ELONGATED QUANTUM DOT CHARGING ENERGIES AND LEVER ARMS

As a first study of EQD formation and the dependence of the high-occupancy charging energy on the EQD length, we study a set of devices with EQD lengths ranging from 240 nm to 1 μm. In this section, for simplicity, lengths refer to nominal gate lengths, whereas in the main text, they refer to lengths overlapping with the Si/SiO$_2$ interface. Out of these devices, we refer to the nominally 360-nm-long polysilicon EQD as device **B**. We use device **B** to estimate the typical EQD charging energies and lever arms $\alpha_{T,T}$ of device **A**. The device schematic for both sets of devices is shown in the top inset of Fig. 7(a): the EQD is connected to three accumulation gates, S, R, and D, via barrier gates B-ST, B-RT, and B-TD. Device **B** is from the same die as device **A**, and the EQD dimensions are the same.

We measure Coulomb diamonds through the S-D channel by applying a varying voltage to the ohmic connected to gate S, and a varying voltage to gate T. Barriers B-ST and B-TD are biased close to their pinch-off voltages, while the accumulation gates S and D are biased significantly above their respective pinch-off voltages. We plot the resulting Coulomb diamonds in Fig. 7(a) (360 nm EQD device).

For each V_T, we find the diamond edges as the $V_{S\text{-Ohmic}}$ values where current is ± 400 pA above the background. Treating upper and lower diamond edges as data traces with setpoints given by V_T, we find peak maxima and minima, which are denoted with cyan and orange points. We manually remove some of the unpaired peaks and dips from the low-electron regime. Ensuring we have an equal number of diamond peaks and dips, we process these to charging energies, shown in Fig. 7(b), and lever arms, shown in Fig. 7(c), using $E_{Ci} = h_i/2$, and $\alpha_{Ti,T} = h_i/(2w_i)$, where h_i and w_i are the height and width of ith diamond, respectively.

We find that the charging energies and lever arms settle to constant value for the last 20 or so measured electrons
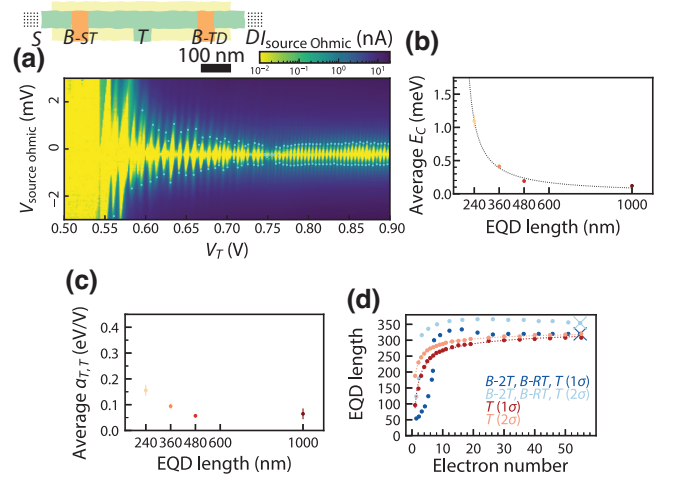

FIG. 7. Elongated quantum dot charging energies and lever arms. (a) Typical Coulomb diamonds from the nominally 360-nm-long EQD device. Device schematic is shown in the top left. The peaks and dips of the automatically detected Coulomb diamonds are shown as cyan circles. (b) Average high-occupancy charging energies as a function of EQD length. (c) Average high-occupancy $\alpha_{T,T}$ lever arms as a function of the EQD length. (d) Simulated EQD length as a function of electron numbers n_T, integrated from the QMED. Red datasets are obtained by only biasing the gate T, and correspond to $(1 - m\sigma)\rho_{\max}$ for $m = 1, 2$ in increasing lightness. Dotted lines are fits to the power law $a n_T^{-1/2} + b$. Blue datasets are obtained by biasing $V_{B\text{-}2T} = 0.275$ V, $V_{B\text{-}RT} = 0.3$ V, and varying V_T, likewise $m = 1, 2$ are shown in increasing lightness. The cross markers correspond to the operating point of Fig. 3(c).

(voltages $V_T = 0.77$ V and above). We find the average charging energy for the last 20 electrons for the 360-nm EQD device to be $E_C = 0.41 \pm 0.02$ meV, and the average lever arm $\alpha_{T,T} = 0.093 \pm 0.005$ eV/V, where error bars are given for one standard deviation. Using the lever arm estimated for device **B**, we obtain the average charging energy $E_C = 0.41 \pm 0.02$ meV for device **A** (data not shown), which agrees well with device **B**.

The high-occupancy average charging energies of the polysilicon devices follow an $1/a$ dependence for length a. This qualitatively agrees with the expectation based on a charged disk. The capacitance of a charged ellipse is given by

$$C = 4\pi\epsilon_r \frac{a}{K\left(a^{-1}\sqrt{a^2 - b^2}\right)}, \tag{D1}$$

where b is the channel width, and K is the complete elliptic integral of the first kind. Here, $K\left(a^{-1}\sqrt{a^2 - b^2}\right)$ approaches a constant value for $a/b \gg 1$, such that the capacitance (D1) behaves as $C \propto a$, and furthermore $E_C \propto 1/C \propto 1/a$.
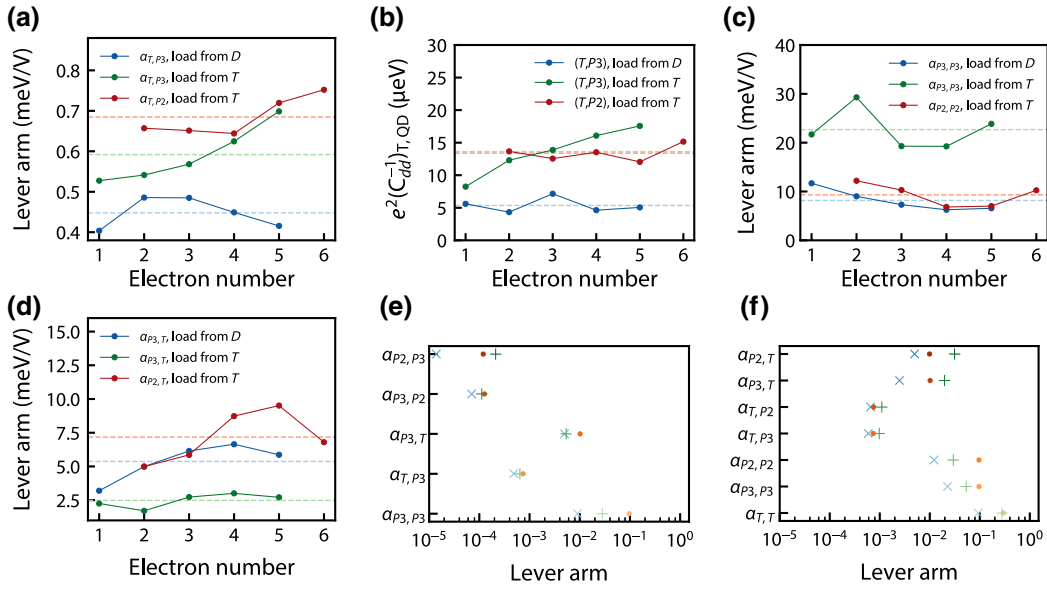
FIG. 8. Experimentally estimated lever arms. Connected datapoints show the estimated (a) $\alpha_{T,P2}$ and $\alpha_{T,P3}$, (b) mutual charging energies between the T QD and the $P3$ or $P2$ QDs, (c) $\alpha_{P2,P2}$ and $\alpha_{P3,P3}$, and (d) $\alpha_{P2,T}$ and $\alpha_{P3,T}$. Dashed lines show averages over electron number. Legends further specify the operating point. (e),(f) Comparison between experimentally estimated and simulated lever arms. Panel (e) shows the lever arms from operating point where the B-$T3$ is off at zero bias, and panel (f) obtained with B-$T3$ on at nonzero bias. Experimentally estimated lever-arm components are drawn with blue diagonal cross markers (x). Lever arms simulated in a fixed operating point, biasing each QD-controlling gate, and without any other gate biases, are drawn with red filled circles. Lever arms simulated with biases at QD controlling gates, and nearest-neighbor gates, are drawn with green plus cross markers (+).

To support the interpretation of a delocalized charge state, and the decrease in the charging energies, we numerically estimate the EQD lengths as a function of electron number. The EQD length, obtained from the simulated 1σ and 2σ QMED contours, is studied for a range of electron numbers, determined by integrating the simulated electron densities for a range of V_T voltages. The results are shown in Fig. 7(d). In a simulation where only the gate T is biased, the EQD length increases monotonically. The EQD length can be fitted to the power law $x_{\text{EQD}} = an_T^{-1/2} + b$, where n_T is the simulated electron number, $a < 0$, and we find $b = 347$ nm and $b = 339$ nm for 1σ and 2σ, respectively.

When B-$2T$ and B-RT are also positively biased with constant voltages, the electron density under B-RT only, $n_{B\text{-}RT} \approx 18.8$, is subtracted from the electron numbers. Here, the EQD length is a more complicated function of the electron number: the more gradual increase at low occupancy is due to how the B-RT gate pulls electrons, and the sharper increase at $n_T \approx 6$ is caused by the EQD density merging with the density under B-$2T$. As the electron number increases further, the EQD length (defined by 1σ or 2σ) gradually decreases due to an increasing concentration of charge in the centre of the QD. The simulated datapoints with $V_T = 0.7093$ V [corresponding to the setpoint from Fig. 3(c)]. The estimated length at this datapoint is $x = 320 \pm 2$ nm at 1σ, and $x = 354 \pm 2$ nm at 2σ.

APPENDIX E: SELF-CONSISTENT SCHRÖDINGER-POISSON AND ELECTROSTATIC SOLVERS

The quantum mechanical electron density (QMED) $n^-(\mathbf{r})$ is defined, as the energy integral of a sum of Fermi-distributed probability densities corresponding to different conduction bands [36]. The QMED can be obtained by iteratively solving the Schrödinger and Poisson equations [36,37], method referred to as self-consistent Schrödinger-Poisson solver (SPS). At convergent energies, the solver outputs both the QMED $n^-(\mathbf{r})$, and the so-called effective-mass probability density $|\Psi_{\alpha,E}(\mathbf{r})|^2$. Total charge associated with an electron density is obtained by integrating $n^-(\mathbf{r})$ over space.

We use an SPS implementation from the semiconductor nanostructure simulation program nextnano++ [36,37]. We model the device gates as 3D Schottky contacts over a silicon (Si) substrate. We take the work function $\phi = 4.05$ eV, consistent with n^{++}-doped polycrystalline silicon. We take the Si/SiO$_2$ interface as a Dirichlet boundary condition, which enforces the electron densities to remain within the Si substrate. We also employ the electrostatics module from the general-purpose simulation software COMSOL Multiphysics, to evaluate the Maxwell capacitance matrix of a system of metallic objects.

We draw the device gate model in COMSOL and nextnano++ layer by layer, using device gate and oxide

dimensions consistent with device design and expected fabricated dimensions. Gate-layer coloring follows the device schematic of Fig. 6(a). At gate overlaps, we draw a gate in the overlapping area, in general creating several, not necessarily connected, objects to describe a single gate. We define higher- and lower-level gate objects as a single electrical node.

To estimate the shape of a QD that is controlled with gate A in an experiment, we bias the gate A and its nearest-neighbor gates in the simulation according to the experimental setpoint, while retaining all other gate biases at zero volts. In these simulated setpoints, we use the SPS to solve for the electron and probability densities. Thus, the simulation has two differences compared to experiments. In the simulation, we do not employ the reservoir gates S, R, and D; and only a subset of the device is biased in one simulation. We split the QD QMED simulation into multiple parts as opposed to simulating all QMEDs in a single simulation for two reasons. High electron densities, such as those due to electron reservoirs S, R, and D, converge more slowly, significantly incresing runtime. Also, in our experiment, we operate plunger gate controlled QDs in the few electron regime, while we operate the EQD at an occupancy of approximately equal to 50–60 electrons. We expect the reservoir electron densities to be approximately a factor of 100 higher than the QD electron densities. Due to the large difference in magnitude, the convergence of the SPS solver depends mostly on the reservoir electron density, leaving the estimate for the QD electron density inaccurate (e.g., simply void of electrons), and significantly different from the estimate obtained without including the reservoir.

We assimilate the QMED with the wave function, as $\rho(\mathbf{r}) = n^-(\mathbf{r})$. We prefer electron densities instead of probability densities to describe the many-electron states in the EQD. Alternatively, we could evaluate probability densities up to the number of electrons we expect at the EQD. Probability densities have orbitals with more irregularity in shape and size as a function of electron number. These states do not account for electron-electron interactions, and hence we do not expect a gain in accuracy by using probability densities. We then consistently employ electron densities for all QD shape estimates.

Shapes of a QD at, e.g., $n\sigma$ are taken as the 3D contour $\mathbf{r}_{\text{boundary}}$ at which the density has fallen by $n\sigma$ from the maximum. That is,

$$\mathbf{r}_{\text{boundary}} = \{\mathbf{r} : \rho(\mathbf{r}) = (1 - n\sigma)\rho_{\max}(\mathbf{r})\}. \quad \text{(E1)}$$

APPENDIX F: LEVER-ARM ESTIMATION

The lever-arm matrix is defined as the product

$$\boldsymbol{\alpha} = -\left(\mathbf{C}_{dd}\right)^{-1} \mathbf{C}_{dg}, \quad \text{(F1)}$$

where $\mathbf{C}_{dd}$ is the dot-dot and $\mathbf{C}_{dg}$ the dot-gate submatrix of the Maxwell capacitance matrix [53]. We use the device **B** high electron number average estimate $\alpha_{T,T} = 0.093 \pm 0.005$ eV/V to convert lever-arm ratios measured in device **A** to lever arms. The slope of a dot-to-reservoir transition on the (V_x, V_y) voltage plane is given by

$$a_i = -\frac{\alpha_{ix}}{\alpha_{iy}}. \quad \text{(F2)}$$

For $i = T$, $x = P2$ $(x = P3)$, and $y = T$, slope estimation with $\alpha_{T,T}$ yields an estimate for $\alpha_{T,P2}$ $(\alpha_{T,P3})$. Using data from Fig. 2, we obtain the lever-arm estimates plotted in Fig. 8(a). Likewise, the intersite charging energies $e^2 \left(\mathbf{C}_{dd}^{-1}\right)_{ij}$ can be estimated from the horizontal and vertical ICT extents ΔV_x and ΔV_y, as

$$\Delta V_x = -2 \left(\mathbf{C}_{dd}^{-1}\right)_{ij} \frac{\alpha_{iy} - \alpha_{jy}}{\alpha_{ix}\alpha_{jy} - \alpha_{iy}\alpha_{jx}} \quad \text{(F3)}$$

$$\Delta V_y = a_{ij} (x_{23} - x_{12}), \quad \text{(F4)}$$

for dots i and j, where a_{ij} is the slope of the ICT. When $\alpha_{P2,P2} \gg \alpha_{T,P2}$, Eq. (F3) simplifies to

$$\Delta V_T = 2|e| \left(\mathbf{C}_{dd}^{-1}\right)_{T,P2} \alpha_{T,T}^{-1}, \quad \text{(F5)}$$

and when $\alpha_{T,T} \gg \alpha_{P2,T}$, Eq. (F4) simplifies to

$$\Delta V_{P2} \approx -2|e| \left(\mathbf{C}_{dd}^{-1}\right)_{T,P2} \alpha_{P2,P2}^{-1}, \quad \text{(F6)}$$

and similarly for $P3$.

The estimates obtained for mutual capacitances $\left(\mathbf{C}_{dd}^{-1}\right)_{T,P2}$ and $\left(\mathbf{C}_{dd}^{-1}\right)_{T,P3}$, and the lever arms $\alpha_{P2,P2}$ and $\alpha_{P3,P3}$ by inverting Eqs. (F5)–(F6) are plotted in Figs. 8(b) and 8(c). Using the above estimates, we may also estimate $\alpha_{P2,T}$ and $\alpha_{P3,T}$ by inverting the ICT slope

$$a_{P2,T} := \frac{\Delta V_T}{\Delta V_{P2}} \quad \text{(F7)}$$

$$= \frac{\alpha_{P2,P2} - \alpha_{T,P2}}{\alpha_{P2,T} - \alpha_{T,T}}. \quad \text{(F8)}$$

The resulting estimates are plotted in Fig. 8(d).

We point out that the setpoint for data in Fig. 3(c) is locally close to the setpoints for the $(P2,T)$ and $(T,P3)$ DQDs discussed in Figs. 2(a) and 2(c), where B-$T3$ is held at zero bias. This is demonstrated by an independent lever-arm ratio estimate. For the charge configurations $(n_{P2}, n_T) = (1, n_T)$ and $(n_T, n_{P3}) = (n_T, 1)$, we extract $\alpha_{T,P2}/\alpha_{T,T} = 0.140 \pm 0.008$ and $\alpha_{T,P3}/\alpha_{T,T} = 0.097 \pm 0.016$, yielding $\alpha_{T,P3}/\alpha_{T,P2} = 0.69 \pm 0.14$, agreeing with the previous estimation. Motivated by this observation, in the following, when simulating the TQD stability

diagram of Fig. 3(c), we use lever arms and intersite charging energies estimated from these DQD datasets.

The above procedure yields estimates for seven out of the nine lever arms for the ($P2,T,P3$) TQD system. The diagonal lever arms $\alpha_{P2,P2}$ and $\alpha_{P3,P3}$ also enable conversion of addition voltages to addition energies. In principle, we may estimate the remaining two from the $P3$ and $P2$ DRTs on the ($P3,P2$) stability diagram. The high resolution along V_{P3} enables estimation of the slope $-\alpha_{P3,P3}/\alpha_{P3,P2}$, whereas the lower resolution along V_{P2} renders estimating $-\alpha_{P2,P3}/\alpha_{P2,P2}$ more difficult. We estimate the latter in a charge configuration of 3 . . . 6 electrons under $P2$ and $P3$, in V_{P2} and V_{P3} range of 0.6 . . . 0.9 V.

APPENDIX G: SIMULATED CAPACITANCE MATRICES

To estimate the Maxwell capacitance matrix **C**, the estimated QD boundaries [Eq. (E1)] are imported to COMSOL as shapes, and defined as a perfect hollow conductor, which is maintained at zero bias. We use the 1σ contours in all our capacitance matrix simulations. Having imported all QD shapes to the same device model, we run the electrostatic solver to obtain **C**. The lever-arm matrix is obtained from Eq. (F1).

As a reference dataset, we calculate a capacitance matrix for the TQD system ($P2,T,P3$), where QD electron densities are obtained in a simulation where only the corresponding plunger gate is biased. We compare this to a simulation, where we account for the effect that barriers have for QD shapes and locations, by biasing a plunger gate and nearest-neighbor barrier gates. We choose the setpoints corresponding to B-$T3$ on and B-$T3$ off (see Figs. 2 and 6).

We plot the simulated lever arms corresponding to the no barrier and B-$T3$ off, as well as the experimentally estimated B-$T3$ off lever arms, in Fig. 8(e). The simulated and experimental lever arms corresponding to no barrier and B-$T3$ on are plotted in Fig. 8(f). We have averaged over charge configurations for the experimental lever arms. We find that the simulated lever arms are systematically larger than experimentally estimated lever arms. Simulations with and without the neighboring barriers produce estimates with similar magnitudes, but simulations with barriers qualitatively follow the trends observed in the experimental lever arms. We associate the systematic mismatch between experimental and simulated lever-arm components to the fact that the simulation systematically overestimates charging energies $|e|\left(\mathbf{C}_{dd}^{-1}\right)_{ij}$, i.e., underestimates the dot-dot capacitances. One source of error is our inability to describe the large electron reservoirs, to which the EQD, and at some setpoints the $P3$ QD, are highly tunnel coupled to. The tunnel coupling affects the QD shape.

In the main text, we summarize these results using the relative error matrix between experimental, $\alpha_{\exp,ij}$, and simulated, $\alpha_{\mathrm{sim},ij}$, lever-arm components, defined as

$$(\delta\alpha)_{ij} = |\alpha_{\exp,ij} - \alpha_{\mathrm{sim},ij}|/|\alpha_{\exp,ij}| \qquad \text{(G1)}$$

[see the lower matrix of Fig. 4(c)].

APPENDIX H: CAPACITIVELY COUPLED TRIPLE QUANTUM DOT STABILITY-DIAGRAM SIMULATION

We simulate the charge-stability diagram of a triple quantum dot as the ground state of the electrostatic Hamiltonian

$$H_{\mathbf{C}} = \sum_{i\in d} \frac{1}{2}\left[\sum_{j\in d} e^2 n_i(\mathbf{C}_{dd}^{-1})_{ij}\, n_j + \sum_{k\in g} e\, n_i \boldsymbol{\alpha}_{ik}V_k\right], \qquad \text{(H1)}$$

where e is the electron charge, n_i the number operator for site i, Δ_i is the site i orbital energy, $(\mathbf{C}_{dd})^{-1}$ the inverse of the dot-dot submatrix of the capacitance matrix, $\boldsymbol{\alpha}$ the lever-arm matrix, and V_k the gate voltage of gate k. We represent the number operators n_i using fermionic ladder operators, in terms of using the Jordan-Wigner mapping. We reduce to considering a single orbital per site (i.e., up to two electrons per site), and, since n_i are diagonal, it suffices to consider $H_{\mathbf{C}}$ as a vector. The ground state is found as the smallest element of the vector. In order to obtain the charge-stability diagram as a function of two voltages, we perform the simulation for a matrix of voltage pairs V_{P2}, V_{P3}. We define the stability diagram as the cross-derivative $\mathrm{d}\left[\mathrm{d}E_g(V_{P2},V_{P3})/\mathrm{d}V_{P3}\right]/\mathrm{d}V_{P2}$, where $E_g(V_{P2},V_{P3})$ is the resulting ground-state matrix as a function of the two voltages.

In the following, matrices are expressed in a basis with indices $\{1,2,3\} = \{P2,T,P3\}$. We use the lever-arm matrix (expressed in units of eV/V) and the inverse dot-dot capacitance matrix in tabulated in Eqs. (1) and (3). The matrix is assumed to be symmetric. We assimilate addition energies to charging energies in this simulation. The elements $|e|\,(\mathbf{C}_{dd})_{P2,P2}^{-1}$ and $|e|\,(\mathbf{C}_{dd})_{P3,P3}^{-1}$ are estimated from the addition energies $\Delta V_{P2}(n \to n+1)$ and $\Delta V_{P3}(n \to n+1)$ of Fig. 3(c), as

$$|e|\,(\mathbf{C}_{dd})_{P2,P2}^{-1} = \frac{1}{2}\alpha_{P2,P2}\Delta V_{P2}(1 \to 2), \qquad \text{(H2)}$$

and likewise for $P3$. The elements $|e|\,(\mathbf{C}_{dd})_{P2,P3}$ and its transpose are not estimated, but a small nonzero element is added to aid matrix inversion. Matrix inversion is used when converting the charging energies to a dot-dot capacitance matrix.
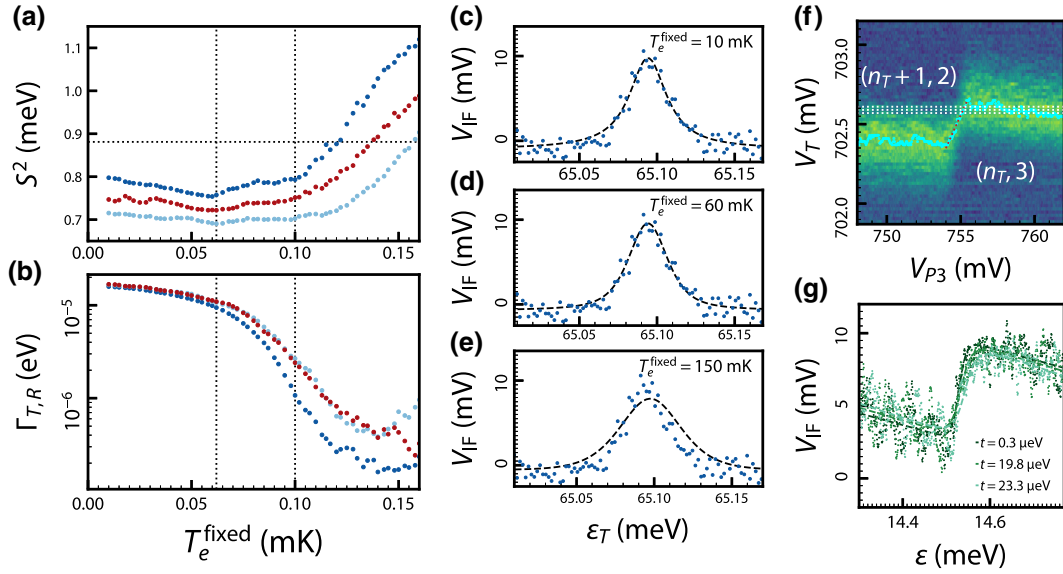
FIG. 9. Electron temperature and tunnel coupling estimation. Colors coincide with the colors used in Fig. 2(c): dark blue for the T-$P3$ system with B-$T3$ on, light blue for T-$P3$ system with B-$T3$ off, and dark red for the T-$P2$ system. (a) Goodness of fit S^2 for a linefit of the sensor DRT to lifetime-broadened $d\langle N\rangle/dE$ (see main text), averaged over the voltage range the linefits were performed. The estimated best temperature, and the estimated upper limit temperature, are denoted as black dotted lines. (b) Corresponding fitted tunnel rate $\Gamma_{T,R}$. (c)–(e) Example datasets (point markers) with linefits (dashed lines) at different fixed temperatures. (f) Example $(T,P3)$ ICT, where the sensor maxima are indicated with cyan circles, tracing out the ICT region. We also indicate the three V_T values we use in the tunnel coupling estimation for this dataset with white dotted lines. (g) Traces along the dotted lines from panel (f) are shown as green-blue data points, and fits to thermal equilibrium $\langle N\rangle$ (see main text) are shown as dashed lines.

To account for finite threshold voltages, we shift plotting ranges for V_{P3} and V_{P2} after the simulation. The simulated ranges are from -0.05 to $+0.25$ V. We use a fixed applied voltage parameter $V_T = 0.0039$ V to set the T QD DRT alignment with respect to the $P2$ and $P3$ DRTs. The resulting simulation is shown in Fig. 4(d). The charge configurations are evaluated as number operator expectation values at each (V_{P2}, V_{P3}) pair, with n_T added for the middle QD charge configuration.

APPENDIX I: ELECTRON TEMPERATURE AND TUNNEL-COUPLING ESTIMATION

We may estimate the electron temperature from the sensor DRT lineshape. We first assert that we are not in a power-broadened regime, by studying the model-independent width of the DRT lineshape as a function of the plunger gate voltages V_{P3} and V_{P2} (data not shown). Here, we observe systematic, nonmonotonic changes in the linewidth as a function of the plunger gate voltages by factors of $\simeq 1.3\dots10$. These dependencies are not analyzed further, but they are expected to be caused by effective changes in the T-R tunnel rate $\Gamma_{T,R}$, since the electron temperature and rf power remain constant over the measurements [54]. This result indicates the linewidth is not thermally broadened and the electron temperature cannot be directly extracted from single lineshape analysis.

However, in the following we present a method to set bounds to the electron temperature of the system.

We fit all the sensor lineshapes between the (1) and (2) occupancies (across a plunger gate voltage range, excluding ICT regions), assuming a fixed temperature, for all temperatures within the set $T_e \in \{0.01,\dots,0.2\}$ K, and evaluate the goodness of fit measure [55, p. 67] $S^2 = \sum_i(y_i - y_i^{\text{fit}})^2/N$, where N is the number of data points in the dataset, y_i are the measured samples, and y_i^{fit} are the corresponding values of the fit function. We repeat this for each three of the datasets from Figs. 2(a) and 2(b), i.e., for the systems T-$P2$, and T-$P3$ with B-$T3$ off and B-$T3$ on. The goodness of fit measure, averaged over the voltage range, for each dataset is shown in Fig. 9(a). The corresponding estimated $\Gamma_{T,R}$ is shown in Fig. 9(b), and example lineshapes with the fits are shown in Figs. 9(c)–9(e). For small temperatures, $\Gamma_{T,R}$ accounts for a significant proportion of the total width, and it is difficult to discern goodness of fit by eye. Nonetheless, the three datasets show a minimum in S at $T_e = 60, 62,$ and 62 mK, respectively, yielding an average best estimate for the electron temperature of $T_e^{\text{best}} = 62$ mK (5.3 μeV). We point out that this is some tens of mK below the typical electron temperature of $\simeq 100$ mK [42]. Since the fit function becomes wider than the lineshape above a threshold temperature [see Fig. 9(e)], the goodness of fit measure degrades above a threshold temperature. We take $T_e^{\text{high}} = 100$ mK (8.6 μeV) as a

threshold temperature, indicated by the change in the slope dS^2/dT_e^{fixed}.

To extract tunnel coupling, we fit each ICT lineshape to the thermal equilibrium charge expectation value

$$\langle N_i \rangle = \text{Tr} \left(\rho_T N_i \right)$$

$$= \frac{1}{2} + n_i + s_i \left\{ \frac{\epsilon}{2E_{+-}} \tanh \left[\frac{E_{+-}}{2k_B T} \right] \right\}, \quad \text{(I1)}$$

where $s_1 = +1$, $s_2 = -1$. Note that this analysis would not be possible without repetition averaging, but in our case, each of the traces is repetition averaged by $N = 10$ times. We show an example closeup of an ICT in Fig. 9(f). The ICT region is found by tracking the sensor peak maxima along V_{P3} (V_{P2} in the respective dataset). We then choose as many traces along V_T as possible within the ICT region, where we have a nonzero signal along V_{P3} (V_{P2}). Besides being limited by sensitivity near the center of the ICT, we discard traces where the sensor lineshape does not have the same slope on both sides of ICT. Using the local lever-arm components [Figs. 8(a) and 8(c)], we convert V_{P3} (V_{P2}) into the detuning, as $\epsilon = e(\alpha_{P3,P3} - \alpha_{T,P3})V_{P3}$. Example traces with the resulting datafits are shown in Fig. 9(g). As can be observed from the spread of the estimated tunnel coupling values in the example dataset, the SNR of the dataset limit our precision.

APPENDIX J: MEDIATED EXCHANGE STRENGTH AND STATE LEAKAGES

Mediated exchange is possible via the so-called Ruderman-Kittel-Kasuya-Yoshida (RKKY) exchange in the charge configuration $(1, 2g, 0e, 1)$, where the middle orbital g represents the highest filled orbital. This mechanism is proposed and analyzed using Schrieffer-Wolff perturbation theory in Ref. [56]. The resulting perturbative Hamiltonian describes the dynamics accurately, when $(1, 2g, 0e, 1)$ is significantly split from $(1, 1g, 1e, 1)$ and $(1, 0g, 2e, 1)$ (by ϵ_{2e}), from $(1, 1, 2)$ and $(2, 1, 1)$ (by $K_i - K_T$), and from $(1, 3, 0)$ and $(0, 3, 1)$ (by ϵ_{2e}). Here, $K_i = |e|^2 (\mathbf{C}_{dd})_{ii}^{-1} /2$ refers to the on-site charging energy at site i (where the index $i = T$ refers to the EQD), and ϵ_{2e} is the next orbital to be filled of the EQD.

The Hamiltonian has the same nonzero elements as the nearest-neighbor exchange Hamiltonian, but with more lengthy terms, even when we disregard Zeeman energy differences, and assume symmetric charging energies $K_{P2} = K_{P3} =: K_i$, and detunings $\epsilon_{P2} = \epsilon_{P3} =: \epsilon_i$. The perturbative mediated exchange strength is then approximately given by

$$J_{121} \approx \frac{4t^4}{2(2K_{ij} - K_i + \frac{1}{2}K_2 + \epsilon_{2g\,1})(K_{ij} - K_i + K_T + \epsilon_{2g\,1})^2}. \quad \text{(J1)}$$
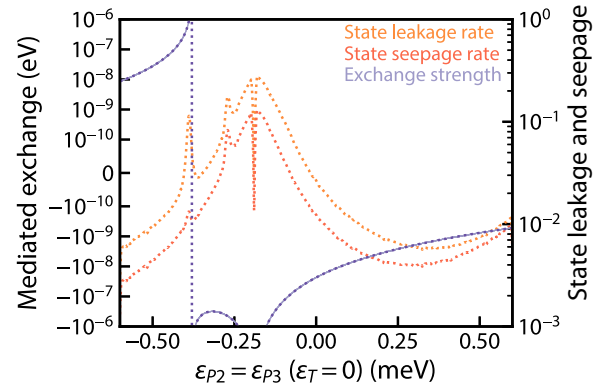

FIG. 10. Mediated exchange strength and state leakages. Mediated exchange strength is evaluated as the matrix element $\langle \uparrow\downarrow \,|H| \downarrow\uparrow \rangle$, numerically (solid purple line) and approximatively analytically (dotted purple line). The orange and red dotted lines indicate state leakage and seepage rates. Parameters used in the simulation: $K_{P2} = K_{P3} = 0.6$ meV, $K_T = 0.4$ meV, $K_{P2,T} = K_{T,P3} = 10\,\mu$eV, $t = 20\,\mu$eV.

Here, we have assumed symmetric EQD-QD tunnel couplings $t = t_{P2,T} = t_{T,P3}$ for convenience. Furthermore, $K_{ij} = |e|^2 (\mathbf{C}_{dd})_{ij}^{-1} /2$ is the inter-site charging energy, and $\epsilon_{2g\,1} = \epsilon_{2g} - \epsilon_1$ is the EQD-QD detuning.

Using the experimentally estimated values for the TQD parameters, we plot the perturbative exchange strength in Fig. 10. We also plot the leakage and seepage rates, evaluated as time averages of [40]

$$L_{\text{out}}(\mathcal{S}) = \text{Tr} \left[P_{1-\mathcal{S}} U \frac{P_{\mathcal{S}}}{d_{\mathcal{S}}} U^\dagger \right], \quad \text{(J2)}$$

$$L_{\text{in}}(\mathcal{S}) = \text{Tr} \left[P_{\mathcal{S}} U \frac{P_{\mathbf{I}-\mathcal{S}}}{d_{\mathbf{I}-\mathcal{S}}} U^\dagger \right], \quad \text{(J3)}$$

where $\mathcal{S}$ and $\mathbf{I} - \mathcal{S}$ are the computational [i.e., $(1, 2g, 0e, 1)$] and leakage [i.e., $(1, 1g, 1e, 1)$, $(1, 0g, 2e, 1)$, $(1, 1, 2)$, $(2, 1, 1)$, $(1, 3, 0)$, and $(0, 3, 1)$] subspaces. The mediated exchange strength exceeds MHz over a range of detunings. However, the exchange rates to states outside the computational subspace also increase, which we expect to limit the fidelity of the operation. At $\epsilon_T = \epsilon_{P2} = \epsilon_{P3} = 0$, where $J_{121} = -17$ MHz, the period-averaged estimated leakage and seepage rates are 0.03 and 0.01, respectively.

[1] M. F. Gonzalez-Zalba, S. de Franceschi, E. Charbon, T. Meunier, M. Vinet, and A. S. Dzurak, Scaling silicon-based quantum computing using CMOS technology, Nat. Electron. **4**, 872 (2021).

[2] X. Xue, M. Russ, N. Samkharadze, B. Undseth, A. Sammak, G. Scappucci, and L. M. K. Vandersypen, Quantum logic with spin qubits crossing the surface code threshold, Nature **601**, 343 (2022).

[3] A. Noiri, K. Takeda, T. Nakajima, T. Kobayashi, A. Sammak, G. Scappucci, and S. Tarucha, Fast universal quantum gate above the fault-tolerance threshold in silicon, Nature **601**, 338 (2022).

[4] A. R. Mills, C. R. Guinn, M. J. Gullans, A. J. Sigillito, M. M. Feldman, E. Nielsen, and J. R. Petta, Two-qubit silicon quantum processor with operation fidelity exceeding 99%, Sci. Adv. **8**, eabn5130 (2022).

[5] E. J. Connors, J. Nelson, and J. M. Nichol, Rapid high-fidelity spin-state readout in Si/Si-Ge quantum dots via rf reflectometry, Phys. Rev. Appl. **13**, 024019 (2020).

[6] K. Takeda, A. Noiri, T. Nakajima, T. Kobayashi, and S. Tarucha, Quantum error correction with silicon spin qubits, Nature **608**, 682 (2022).

[7] S. G. Philips, M. T. Mądzik, S. V. Amitonov, S. L. de Snoo, M. Russ, N. Kalhor, C. Volk, W. I. Lawrie, D. Brousse, and L. Tryputen, Universal control of a six-qubit quantum processor in silicon, Nature **609**, 919 (2022).

[8] L. L. Guevel, G. Billiot, X. Jehl, S. De Franceschi, M. Zurita, Y. Thonnart, M. Vinet, M. Sanquer, R. Maurand, A. G. M. Jansen, and G. Pillonnet, in *2020 IEEE International Solid- State Circuits Conference - (ISSCC)* (IEEE, San Fransisco, CA, USA, 2020), p. 306.

[9] A. Ruffino, T.-Y. Yang, J. Michniewicz, Y. Peng, E. Charbon, and M. F. Gonzalez-Zalba, cryo-CMOS chip that integrates silicon quantum dots and multiplexed dispersive readout electronics, Nat. Electron. **5**, 53 (2022).

[10] M. Veldhorst, C. H. Yang, J. C. C. Hwang, W. Huang, J. P. Dehollain, J. T. Muhonen, S. Simmons, A. Laucht, F. E. Hudson, K. M. Itoh, *et al.*, A two-qubit logic gate in silicon, Nature **526**, 410 (2015).

[11] D. M. Zajac, A. J. Sigillito, M. Russ, F. Borjans, J. M. Taylor, G. Burkard, and J. R. Petta, Resonantly driven CNOT gate for electron spins, Science **359**, 439 (2017).

[12] W. Huang, C. H. Yang, K. W. Chan, T. Tanttu, B. Hensen, R. C. C. Leon, M. A. Fogarty, J. C. C. Hwang, F. E. Hudson, K. M. Itoh, A. Morello, A. Laucht, and A. S. Dzurak, Fidelity benchmarks for two-qubit gates in silicon, Nature **569**, 532 (2019).

[13] M. Veldhorst, H. G. J. Eenink, C.-H. Yang, and A. S. Dzurak, Silicon CMOS architecture for a spin-based quantum computer, Nat. Commun. **8**, 1 (2017).

[14] J. M. Boter, J. P. Dehollain, J. P. G. Van Dijk, Y. Xu, T. Hensgens, R. Versluis, H. W. L. Naus, J. S. Clarke, M. Veldhorst, F. Sebastiano, and L. M. K. Vandersypen, Spiderweb array: A sparse spin-qubit array, Phys. Rev. Appl. **18**, 024053 (2022).

[15] B. Undseth, X. Xue, M. Mehmandoost, M. Rimbach-Russ, P. T. Eendebak, N. Samkharadze, A. Sammak, V. V. Dobrovitski, G. Scappucci, and L. M. Vandersypen, Non-linear response and crosstalk of electrically driven silicon spin qubits, Phys. Rev. Appl. **19**, 044078 (2023).

[16] P. Lafarge, H. Pothier, E. R. Williams, D. Esteve, C. Urbina, and M. H. Devoret, Direct observation of macroscopic charge quantization, Zeitschrift für Physik B Condens. Matter **85**, 327 (1991).

[17] M. G. House, I. Bartlett, P. Pakkiam, M. Koch, E. Peretz, J. V. D. Heijden, T. Kobayashi, S. Rogge, and M. Y. Simmons, High-sensitivity charge detection with a single-lead quantum dot for scalable quantum computation, Phys. Rev. Appl. **6**, 044016 (2016).

[18] M. Urdampilleta, D. J. Niegemann, E. Chanrion, B. Jadot, C. Spence, P.-A. Mortemousque, C. Bäuerle, L. Hutin, B. Bertrand, S. Barraud, R. Maurand, M. Sanquer, X. Jehl, S. De Franceschi, M. Vinet, and T. Meunier, Gate-based high fidelity spin readout in a CMOS device, Nat. Nanotechnol. **14**, 737 (2019).

[19] V. N. Ciriano-Tejel, M. A. Fogarty, S. Schaal, L. Hutin, B. Bertrand, L. Ibberson, M. F. Gonzalez-Zalba, J. Li, Y. -M. Niquet, M. Vinet, and J. J. Morton, Spin Readout of a CMOS quantum dot by gate reflectometry and spin-dependent tunneling, PRX Quantum **2**, 010353 (2021).

[20] G. Oakes, V. Ciriano-Tejel, D. Wise, M. Fogarty, T. Lundberg, C. Lainé, S. Schaal, F. Martins, D. Ibberson, L. Hutin, *et al.*, Fast high-fidelity single-shot readout of spins in silicon using a single-electron box, Phys. Rev. X **13**, 011023 (2023).

[21] D. J. Niegemann, V. El-Homsy, B. Jadot, M. Nurizzo, B. Cardoso-Paz, E. Chanrion, M. Dartiailh, B. Klemt, V. Thiney, C. Bäuerle, *et al.*, Parity and singlet-triplet high-fidelity readout in a silicon double quantum dot at 0.5 K, PRX Quantum **3**, 040335 (2022).

[22] F. Martins, F. K. Malinowski, P. D. Nissen, S. Fallahi, G. C. Gardner, M. J. Manfra, C. M. Marcus, and F. Kuemmeth, Negative spin exchange in a multielectron quantum dot, Phys. Rev. Lett. **119**, 227701 (2017).

[23] F. K. Malinowski, F. Martins, T. B. Smith, S. D. Bartlett, A. C. Doherty, P. D. Nissen, S. Fallahi, G. C. Gardner, M. J. Manfra, C. M. Marcus, and F. Kuemmeth, Spin of a multi-electron quantum dot and its interaction with a neighboring electron, Phys. Rev. X **8**, 011045 (2018).

[24] Z. Wang, M. Feng, S. Serrano, W. Gilbert, R. C. Leon, T. Tanttu, P. Mai, D. Liang, J. Y. Huang, Y. Su, *et al.*, Jellybean quantum dots in silicon for qubit coupling and on-chip quantum chemistry, Adv. Mater. **0**, 2208557 (2023).

[25] F. K. Malinowski, F. Martins, T. B. Smith, S. D. Bartlett, A. C. Doherty, P. D. Nissen, S. Fallahi, G. C. Gardner, M. J. Manfra, C. M. Marcus, and F. Kuemmeth, Fast spin exchange across a multielectron mediator, Nat. Commun. **10**, 1 (2019).

[26] Z. Cai, M. A. Fogarty, S. Schaal, S. Patomäki, S. C. Benjamin, and J. J. L. Morton, A silicon surface code architecture resilient against leakage errors, Quantum **3**, 212 (2019).

[27] N. I. Dumoulin Stuyck, R. Li, C. Godfrin, A. Elsayed, S. Kubicek, J. Jussot, B. T. Chan, F. A. Mohiyaddin, M. Shehata, G. Simion, Y. Canvel, L. Goux, M. Heyns, B. Govoreanu, and I. P. Radu, in *2021 Symposium on VLSI Circuits* (IEEE, Kyoto, Japan, 2021), p. 1.

[28] M. Veldhorst, J. C. C. Hwang, C. H. Yang, J. P. Dehollain, J. T. Muhonen, F. E. Hudson, K. M. Itoh, A. Morello, and A. S. Dzurak, An addressable quantum dot qubit with fault-tolerant control-fidelity, Nat. Nanotechnol. **9**, 981 (2014).

[29] Electronic access: https://www.qdevil.com.

[30] F. Vigneau, F. Fedele, A. Chatterjee, D. Reilly, F. Kuemmeth, M. F. Gonzalez-Zalba, E. Laird, and N. Ares, Probing

quantum devices with radio-frequency reflectometry, Appl. Phys. Rev. **10**, 021305 (2023).

[31] M. F. Gonzalez-Zalba, S. Barraud, A. J. Ferguson, and A. C. Betz, Probing the limits of gate-based charge sensing, Nat. Commun. **6**, 1 (2015).

[32] W. H. Lim, C. H. Yang, F. A. Zwanenburg, and A. S. Dzurak, Spin filling of valley-orbit states in a silicon quantum dot, Nanotechnology **22**, 335704 (2011).

[33] D. Keith, M. G. House, M. B. Donnelly, T. F. Watson, B. Weber, and M. Y. Simmons, Single-shot spin readout in semiconductors near the shot-noise sensitivity limit, Phys. Rev. X **9**, 041003 (2019).

[34] D. J. Ibberson, T. Lundberg, J. A. Haigh, L. Hutin, B. Bertrand, S. Barraud, C.-M. Lee, N. A. Stelmashenko, G. A. Oakes, L. Cochrane, J. W. Robinson, M. Vinet, M. F. Gonzalez-Zalba, and L. A. Ibberson, Large dispersive interaction between a CMOS double quantum dot and microwave photons, PRX Quantum **2**, 020315 (2021).

[35] S. Schaal, I. Ahmed, J. A. Haigh, L. Hutin, B. Bertrand, S. Barraud, M. Vinet, C.-M. Lee, N. Stelmashenko, J. W. A. Robinson, J. Y. Qiu, S. Hacohen-Gourgy, I. Siddiqi, M. F. Gonzalez-Zalba, and J. J. L. Morton, Fast gate-based readout of silicon quantum dots using Josephson parametric amplification, Phys. Rev. Lett. **124**, 067701 (2020).

[36] S. Birner, *Modeling of semiconductor nanostructures and semiconductor-electrolyte interfaces*; Technische Universität München, 2011. https://www.osti.gov/etdeweb/biblio/21538992.

[37] nextnano++ manual. nextnano.de/manual/nextnanoplus, https://www.nextnano.de/manual/nextnanoplus/index.html. Accessed: 2022-11-08.

[38] C. H. Yang, A. Rossi, N. S. Lai, R. C. C. Leon, W. H. Lim, and A. S. Dzurak, Charge state hysteresis in semiconductor quantum dots, Appl. Phys. Lett. **105**, 183505 (2014).

[39] F. Fedele, *Spin interactions within a two-dimensional array of GaAs double dots*; Niels Bohr Institute, 2020. https://nbi.ku.dk/english/theses/phd-theses/federico-fedele/.

[40] C. J. Wood and J. M. Gambetta, Quantification and characterization of leakage errors, Phys. Rev. A **97**, 032306 (2018).

[41] T. Ando, A. B. Fowler, and F. Stern, Electronic properties of two-dimensional systems, Rev. Mod. Phys. **54**, 437 (1982).

[42] L. DiCarlo, H. Lynch, A. Johnson, L. Childress, K. Crockett, C. Marcus, M. Hanson, and A. Gossard, Differential charge sensing and charge delocalization in a tunable double quantum dot, Phys. Rev. Lett. **92**, 226801 (2004).

[43] T. Tanttu, W. H. Lim, J. Y. Huang, N. D. Stuyck, W. Gilbert, R. Y. Su, M. Feng, J. D. Cifuentes, A. E. Seedhouse,

and S. K. Seritan, Consistency of high-fidelity two-qubit operations in silicon, arXiv:2303.04090v2.

[44] J. Yoneda, W. Huang, M. Feng, C. H. Yang, K. W. Chan, T. Tanttu, W. Gilbert, R. Leon, F. Hudson, K. Itoh, *et al.*, Coherent spin qubit transport in silicon, Nat. Commun. **12**, 4114 (2021).

[45] A. Noiri, K. Takeda, T. Nakajima, T. Kobayashi, A. Sammak, G. Scappucci, and S. Tarucha, A shuttling-based two-qubit logic gate for linking distant silicon quantum processors, Nat. Commun. **13**, 5740 (2022).

[46] I. Seidler, T. Struck, R. Xue, N. Focke, S. Trellenkamp, H. Bluhm, and L. R. Schreiber, Conveyor-mode single-electron shuttling in Si/SiGe for a scalable quantum computing architecture, npj Quantum Inf. **8**, 1 (2022).

[47] W. Gilbert, A. Saraiva, W. H. Lim, C. H. Yang, A. Laucht, B. Bertrand, N. Rambal, L. Hutin, C. C. Escott, M. Vinet, *et al.*, Single-electron operation of a silicon-CMOS 2× 2 quantum dot array with integrated charge sensing, Nano Lett. **20**, 7882 (2020).

[48] J. Duan, M. A. Fogarty, J. Williams, L. Hutin, M. Vinet, and J. J. Morton, Remote capacitive sensing in two-dimensional quantum-dot arrays, Nano Lett. **20**, 7123 (2020).

[49] F. Borjans, X. G. Croot, X. Mi, M. J. Gullans, and J. R. Petta, Resonant microwave-mediated interactions between distant electron spins, Nature **577**, 195 (2020).

[50] P. Harvey-Collard, J. Dijkema, G. Zheng, A. Sammak, G. Scappucci, and L. M. K. Vandersypen, Coherent spin-spin coupling mediated by virtual microwave photons, Phys. Rev. X **12**, 021026 (2022).

[51] I. Siddiqi, Engineering high-coherence superconducting qubits, Nat. Rev. Mater. **6**, 875 (2021).

[52] D. Bluvstein, S. J. Evered, A. A. Geim, S. H. Li, H. Zhou, T. Manovitz, S. Ebadi, M. Cain, M. Kalinowski, D. Hangleiter, *et al.*, Logical quantum processor based on reconfigurable atom arrays, Nature **0**, 1 (2023).

[53] A. R. Mills, D. M. Zajac, M. J. Gullans, F. J. Schupp, T. M. Hazard, and J. R. Petta, Shuttling a single charge across a one-dimensional array of silicon quantum dots, Nat. Commun. **10**, 1 (2019).

[54] I. Ahmed, A. Chatterjee, S. Barraud, J. J. L. Morton, J. A. Haigh, and M. F. Gonzalez-Zalba, Primary thermometry of a single reservoir using cyclic electron tunneling to a quantum dot, Commun. Phys. **1**, 66 (2018).

[55] G. Cowan, *Statistical Data Analysis* (Oxford University Press, 1998).

[56] V. Srinivasa, H. Xu, and J. M. Taylor, Tunable spin-qubit coupling mediated by a multielectron quantum dot, Phys. Rev. Lett. **114**, 226803 (2015).